International Journal of Heat and Mass Transfer 52 (2009) 4047–4062

Contents lists available at ScienceDirect

International Journal of Heat and Mass Transfer

journal homepage: www.elsevier.com/locate/ijhmt

Vortices and heat flux around a wall-mounted cube cooled simultaneously by a jet and a crossflow

M. Popovac [1], K. Hanjalić *

Department of Multi-Scale Physics, Delft University of Technology, Lorentzweg 1, 2628 CJ Delft, The Netherlands

ARTICLE INFO

Article history:
Received 5 December 2008
Accepted 23 March 2009
Available online 4 May 2009

Keywords:
Cube in a crossflow
Impinging jet
Vortex morphology
Heat transfer

ABSTRACT

Vortex morphology and heat transfer over a wall-mounted heated cube in an in-line array, cooled simultaneously by a crossflow and a normally impinging round jet, have been studied by conjugate large-eddy simulations. The interaction of the two streams and the cubes leads to the formation of complex vortical structures that govern heat removal from the cube surface. The strongest and the most evenly distributed cooling were found on the cube top and the front face. The heat flux on the side faces is lower in the zones where the flow separates, while it increases downstream where a fresh fluid from the crossflow flushes the faces. The separation on the back face of the cube creates an arch vortex, which dictates the heat transfer from that face. Despite its persistence and relative steadiness, significant nonuniformity of the temperature field has been detected on the rear face, characterised by the time meandering of hot spots. Vortex rings, created in the jet shear layer before its impact on the cube, break up upon impingement, leading to the re-establishing of the thermal boundary layer, and the consequent enhancement of heat transfer. The turbulent heat flux and its budget correlate well with the corresponding turbulent stress components.

1. Introduction

Local overheating due to concentrated power dissipation has been regarded as one of the chief limitations to further increase of performance and to size miniaturisation of chips and other electronics components. Enhancing and a better control of heat transfer are also still the main challenges in gas turbines (cooling of turbine blades and walls of the combustion chambers), as well as in various types of compact heat exchangers and many other devices and equipment in thermal and process industries. The problem is not only in removing very high heat rates, but also in achieving cooling (or heating) uniformity and thus preventing the local hot spots that cause thermal fatigue and material damage. The classic methods of predicting heat transfer, practiced still in industrial design, have long reached their limitations and the new challenges call for more detailed field studies that will make it possible to better understand the subtle mechanism of local heat transfer in complex geometries and the role therein of the vortical structure and turbulence. In other words, accurate information on the local velocity and temperature field, their mutual interactions and effects on heat transfer in various configurations are the key prerequisites for the novel and improved design that will overcome the present limitations.

This study aims at contributing to the above goal. We performed large-eddy simulation (LES) of turbulent convective cooling of a simplified electronic component in an array, subjected to a crossflow and an impinging jet. The configuration consists of an in-line array of five cubes mounted on the wall of a plane channel, with the central cube internally heated. The heat generated electrically in the cube copper core, emerges through the protective low-conducting epoxy layer (found also in real electronic components), and it is then removed through the outer surface of the cube by the bulk flow (referred below as a "crossflow") in the channel and a normally impinging round jet with its axis aligned with the cube front face. Apart from the cubic shape (adopted on purpose to serve as a reference for comparison and further studies), the configuration mimics in all respects the cooling of electronic components and is also relevant to internal cooling of gas-turbine blades and to other heat transfer applications. Because of direct interaction between the fluid flow and heat conduction through the epoxy layer, the simultaneous, conjugate computations were performed generating instantaneous three-dimensional velocity and temperature field around the cube, and the latter also in the cube interior and on the solid–fluid interface. This made it possible to identify the governing vortical, turbulence and plume structures around the cube, their signature on the cube surface and effect on the temperature distribution and heat transfer through the cube protective layer.

* Corresponding author. Present address: Marie Curie Chair, Dept of Mechanics and Aeronautics, "Sapienza" University of Rome, Rome, Italy.
E-mail address: hanjalic@dma.ing.uniroma1.it (K. Hanjalić).
[1] Present address: Arsenal Research, Sustainable Energy Systems, Giefinggasse 2, 1210 Vienna, Austria.

0017-9310/$ - see front matter © 2009 Elsevier Ltd. All rights reserved.
doi:10.1016/j.ijheatmasstransfer.2009.03.042

The present simulations mimic closely (though with some small difference in the jet displacement) the experimental set-up of Tummers et al. [1], who reported on the measurements of the velocity and turbulence field using the particle-image velocimetry (PIV) and of the temperature on the central cube surface using liquid crystal thermography. While LES of this configurations have already been reported by Popovac and Hanjalić [2], focusing on the velocity field, the flow pattern, turbulence structure and its statistics, in this paper we focus on the vortex morphology, thermal field and heat transfer. The study draws from prior LES of flow in a similar configuration, but without jet, Ničeno et al., [3], Ničeno and Hanjalić, [4], and from LES of a round jet impinging normally on a heated flat plate, Hadžiabdić and Hanjalić, [5]. All simulations mentioned above have been performed with the same in-house unstructured finite volume computational code *T-FlowS*.

2. Flow description and computational issues

The flow configuration, together with discussion of the choice of the solution domain, inflow and boundary conditions and computational aspects, have been described in details in [2]. Here it will suffice to summarize the main features and specification of parameters.

2.1. Flow configuration, solution domain and computational mesh

Five cubes, denoted as C1–C5, are mounted on the bottom wall of a plane channel, in line with the bulk flow, Fig. 1. The central cube *C3* is internally heated and cooled by the channel ("cross") flow as well as by a round jet issuing from an upstream-displaced circular orifice in the upper channel wall, which connects the channel and the plenum chamber.

All dimensions are specified in terms of the height of the cube of $h = 15$ mm: the height of the channel is $H = 2h$, the distance between the cube centres is $d = 4h$, the diameter of the orifice $D = 0.8h$, and the orifice height $n = 0.4h$. In order to make it possible to neglect the effects of the side walls, as achieved in the experiment of Tummers et al. [1], the spanwise channel width in the computation was set to $W = 7h$. The simulations have been performed for a scaled geometry with its size normalised with h. Consequently the physical parameters (e.g. viscosity) were adjusted to maintain the specified Reynolds number.

The preliminary experiment of Flikweert [6], aimed at establishing the optimum positioning of the jet with respect to the cube, showed that the maximum cooling effect of the central cube was achieved when the jet axis was moved upstream from the cube *C3* centre by a distance $S' = 0.53h$ (8 mm), as shown Fig. 2. Subsequently, detailed experiments were performed by Tummers et al. [1] for this configuration. However, in order to make the mesh generation somewhat easier, in the present computation the axis of the orifice is aligned with the leading edge of the central cube *C3*: the orifice axis is thus shifted by $S = 0.5h$ (7.5 mm) upstream from the centre of *C3*. For this reason the origin of the coordinate system is also placed where the axis of the orifice intersects with the bottom wall, as shown in Fig. 1. It was thought originally that this small mismatch of 0.5 mm in the positions of the jet centre

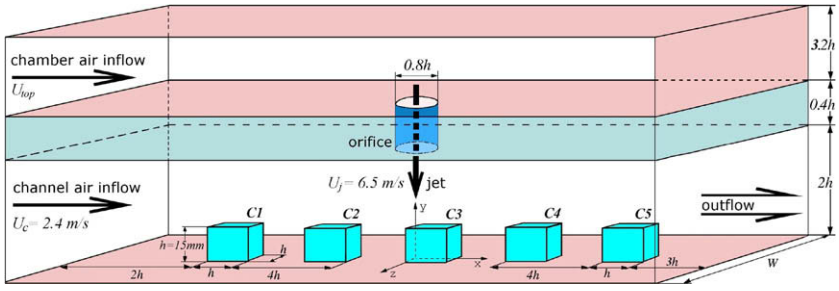

Fig. 1. Schematics of the configuration studied, indicating the coordinate system, dimensions and the imposed reference bulk velocities.

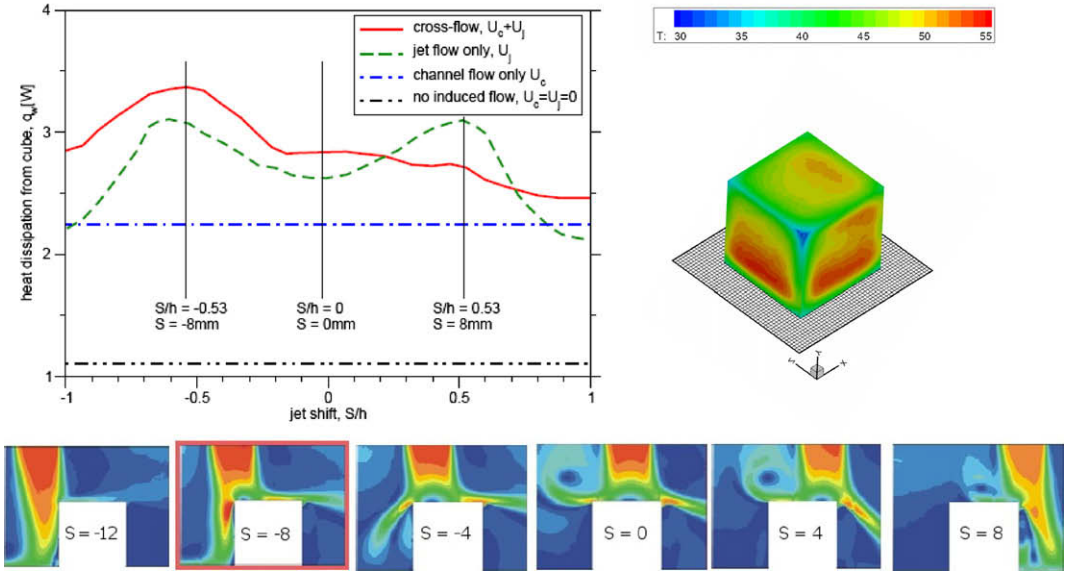

Fig. 2. (Above) Overall heat loss from the central cube for different flow regimes and different positions of the impinging jet (left) and a view from the back of the thermographic image of the cube temperature surface for the optimum cooling jet positioning (right). (Below) PIV velocity field in the midplane for different positioning (in mm) of the jet with respect to the cube (from the experiments of Tummers et al. [1], see also Flikweert [6]).

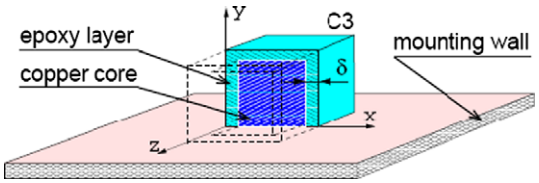

Fig. 3. A sketch of the composition of the central heated cube *C3*.

with respect to the cube will not matter much. However, this assumptions proved not to be fully justified because the splitting of the jet mass and momentum between the upstream part washing the front face and the downstream part impinging on the cube changed sufficiently (about 10% in the momentum) to cause some noticeable discrepancies between the LES and experimental results, as discussed below.

The Reynolds (Re) numbers considered are in the range of the typical values encountered in real electronic cooling systems. The Re number of the channel flow, based on its bulk velocity U_c (2.4 m/s) and the channel height H, is $Re_c = 4800$. Similar is the jet Re number $Re_j = 5200$, based on its bulk velocity U_j (6.5 m/s) and the diameter of the orifice D. Apart from the jet Re number, the important parameter for the impingement characteristics is the orifice-to-cube distance, which in the present case is $h/D = 1.25$. The flow pattern of the jet in the crossflow is primarily influenced by the mass flux ratio of the two flows, $\alpha_m = (\rho_j U_j^2/\rho_c U_c^2)^{1/2}$. In the present case the densities are the same, and the mass flux ratio reduces to the velocity ratio $\alpha_v = U_j/U_c = 2.7$.

The composition of the central cube *C3* is illustrated in Fig. 3, and a summary of the physical properties for the materials is given in Table 1 (it should be noted that different values of the properties were used in the computations in order to maintain the required Re number, because the geometry was scaled with the cube height). The cube *C3* consists of an electrically heated copper core, coated with $\delta = 0.1\ h$ (1.5 mm) thick low-conducting epoxy mantle. It is the same cube that was used in the experiment of Meinders and Hanjalić [7]. The copper core is kept at a constant temperature of $\Theta_{Cu} = 70\ ^\circ C$. Since the thermal resistance of epoxy is much larger than that of copper, it is assumed that the temperature throughout the copper core, and hence at the inner face of the epoxy layer, is uniform and constant. This cube composition corresponds to a real electronic component, since in practice the microprocessors, heated inside by transistors, are covered with a protective coating, and cooled by a fluid flow from the outside. Other cubes in the row served to provide the velocity and turbulence fields pertinent to a real configuration of electronic components.

The ratio of the heat transfer properties of the fluid and solid in contact $K = [(\rho c_p \lambda)_f/(\rho c_p \lambda)_s]^{1/2}$ can be used to define the thermal interactivity of the two media, representing the heat transfer dynamics from the surface of the solid to the surrounding fluid. For the combination air – epoxy this thermal activity ratio is $K = 8.14 \times 10^{-3}$. Such a low value of K means that the temperature fluctuations in the fluid are negligibly small at the solid–fluid interface (Kasagi et al. [8]), which is otherwise typical for the constant temperature boundary condition. Still, specifying the temperature at the interior boundary of the copper core is different from specifying either temperature or heat flux on the fluid boundary, because it allows the temperature at the surface to develop naturally following the local flow conditions.

Table 1
Properties of the materials occurring in the computations.

	Air	Epoxy	Copper
Specific heat capacity (c_p)	1.01 $\times 10^3$ m^2/s^2 K	1.67 $\times 10^3$ m^2/s^2 K	3.80 $\times 10^2$ m^2/s^2 K
Thermal conductivity (λ)	2.57 $\times 10^{-2}$ kg m/s^{3}K	2.36 $\times 10^{-1}$ kg m/s^{3}K	4.01 $\times 10^2$ kg m/s^3 K
Kinematic viscosity (ν)	1.567 $\times 10^{-5}$ m^2/s	–	–
Density (ρ)	1.16 kg/m^3	1.15 $\times 10^3$ kg/m^3	8.92 $\times 10^3$ kg/m^3

In order to reproduce the experimental conditions as close as possible, the solution domain was chosen to coincide with the experimental test section, as shown in Fig. 1. It encompasses the channel with all five cubes, portions of the channel before and after cubes in length of 2 *h* and 3 *h* respectively, as well as the plenum chamber from which the jet is issued. Because of a complex flow structures and geometry, the computational mesh was carefully optimised in order to minimise the number of cells while still achieving sufficient mesh resolution especially around *C3* cube. For each of the cubes and for the plenum chamber a separate subdomain was considered making it possible to adequately mesh each flow region. The mesh around the *C3* cube was composed of several imbedded meshes containing predominantly hexahedral cells with triangular prisms used at subdomains interfaces. By clustering the mesh towards the edges of the cubes, a finer resolution in the critical near-wall region was achieved. In order to reduce the total number of cells, the mesh is paved with somewhat larger cells further away in the spanwise direction, but with a layer of fine cells clustered near the side boundaries. The same paving method was used to connect the cube subdomains with different spacing in the direction along the channel height. The mesh in the solid part of the domain was extruded from the fluid–solid interface in five layers. This meshing strategy allowed to have hexahedral cells next to all boundaries, which improves the numerical accuracy (especially of the wall friction and heat transfer) and the stability of the computation. The total number of cells was 8.5×10^6. The mesh cell dimensions (normalised by wall units) in the region of 1 *h* around the central cube, which is of the prime interest, were roughly $\mathcal{O}(\Delta x^+) = O(\Delta z^+) = O(\Delta y^+) = 10 L_{Kol}$, where L_{Kol} is the Kolmogorov length scale. A-*posteriori* evaluation of the ratio of the subgrid-scale to molecular viscosity at several monitoring locations close to the walls were all within the recommended limit of $\nu_t/\nu \approx 10 \div 20\%$. More details of the mesh resolution can be found in [2].

2.2. Initial and boundary conditions

The no-slip velocity boundary condition was applied on all walls, including the side walls at $y/h = 3.5$ in the channel containing cubes. At the downstream boundary of the channel the gradients of all variables in the streamwise direction are set to zero. The constant temperature $\Theta_w = 20\ ^\circ C$ was imposed on all walls, apart from the inner wall of the epoxy layer of the central heated cube: there the temperature was set to the value of the copper core $\Theta_{Cu} = 70\ ^\circ C$. Although highly preferable from numerical stability and accuracy point of view, periodic boundary condition could not be applied in this computation. In order to speed-up the computation, the velocity and temperature field was initialized with the solution from RANS calculation on the same geometry and with the same boundary conditions.

The structure and the parameters of an impinging jet depend strongly on the flow conditions upstream of the jet. Initial attempts to use the available limited information from the experiment (velocity and turbulence intensity profiles at the jet exit), resulted in a markedly different flow pattern in the jet interaction with the cross stream and consequently around the cube, indicating the need to simulate the flow far upstream from the jet exit (for details see Popovac [9]). To that purpose, a plenum chamber was added to the computational domain. This top chamber was closed with

walls at three sides, with a height of $4D$ and a width of $4D \times 4D$, and was connected through a circular (jet) orifice to the channel containing the cubes, so that all incoming fluid passed through the jet. Such a semi-closed chamber was considered to be large enough to mimic the open chamber in the experiment, allowing to ignore any influence of the side walls on the jet formation. In the experiment [1] the bulk inflow information is extracted from the mass flow rate, and subsequently checked from the velocity measurements. The channel flow had the mass flow rate of $m_c = 2.5 \times 10^{-2}$ kg/s that gave its bulk velocity $U_c = 2.4$ m/s, and the jet mass flow rate was $m_j = 8.5 \times 10^{-4}$ kg/s resulting in its bulk velocity $U_j = 6.5$ m/s.

The inflow boundary conditions both for the channel and plenum chamber were obtained from LES of a fully developed turbulent isothermal ($\Theta_{in} = \Theta_w = 20$ °C) channel flow, which were run simultaneously with the computation of the rest of the flow. Admittedly, in the experiment the channel flow was not fully developed, but the two cubes preceding the *C3* cube, which was in focus of our simulations, generated sufficiently strong vortical structures and turbulence level to compensate for the imperfect mimicking of the channel inflow conditions. The parameters by which the computational inflow conditions were matched with the experimental ones are the bulk velocities, i.e. the Reynolds numbers of the two flows.

2.3. Numerical and modelling details

The LES here reported was performed using *T-FlowS*, the in-house unstructured collocated control-volume-based Navier–Stokes solver, Ničeno and Hanjalić [4]. The subgrid scale stresses (SGS) were calculated from the dynamic Smagorinsky model of Germano et al. [10], hence no defining of the Smagorinsky constant was needed, and no wall damping nor wall functions were used. The time step, normalised with the cube height and fluid viscosity, was set to $\Delta t_{nor} = \nu \Delta t / h^2 = 1.33 \times 10^{-6}$. This gave a typical Courant–Friedrich–Levy (CFL) number around 0.7, and only in isolated regions of high velocity CFL reached a peak value around 2. For the convective scheme, a full central differencing (CDS) was used, and no problems with the numerical stability have been observed. However, in the iterative solution of the transport equations a slight under-relaxation was applied using the under-relaxation factor of 0.9 for the momentum and temperature equations and 0.8 for the pressure correction. The time marching was performed using a fully-implicit three-level time scheme. An iterative pressure correction algorithm was used for the pressure-velocity coupling, and the diagonally preconditioned conjugate gradient (CG) method was used for solving the linearised system of equations.

In the channel flow simulation that was run simultaneously to generate the inflow data, the pressure drop was recalculated after each time step from the difference between the imposed mass flux m_0 and the currently calculated m_1. This resulted in a small variation of the Reynolds number of the computed flow, $\Delta Re/Re \approx 1\%$. The computation was initiated with the RANS mean flow field, yet in the first $4t_{ft}$, where $t_{ft} = h/U_j$ is the *flow-through time* based on the bulk velocity of the jet and the height of the cube, the statistics was not gathered in order to let the flow structures develop naturally. After this initial phase the results were averaged over the normalised averaging time of 10 t_{ft}, which corresponds to the time normalised with the cubes' height and fluid viscosity $t_{nor} = \nu\ t/h^2 = 1.5 \times 10^{-2}$. This averaging time was also needed to get the temperature field developed, since the computation of the heat conduction in the epoxy layer takes more time due to the much lower heat diffusivity of the epoxy material. Furthermore, in order to develop faster the temperature field in the solid part of the cube, the thermal diffusivity of epoxy was set initially to be ten times higher, and gradually decreased to its real value during the computation.

3. Results and discussion

3.1. Flow field and vortex morphology

A detailed discussion of the general flow pattern and turbulence field has been reported in [2]. The focus here is on vortex morphology in the jet and around the cube and their signature in the temperature field and effects on heat transfer from the central cube. The contours of the time-averaged velocity magnitude in Fig. 4a show the overall flow pattern in the vertical midplane, $z/h = 0$. The main feature of the flow is the jet splitting into two parts, one washing the front face of the cube and subsequently impinging on the bottom channel wall, and the other impinging on the cube top surface. A characteristic horseshoe vortex is formed in front of the cube, which splits again into two parts on both cube sides, one that reattaches to the cube side walls after small separation bubbles at the leading edges, and the other part that is being deflected away from the cube.

One can identify several characteristic flow zones in the jet-cube assembly, as denoted in Fig. 4b which shows velocity vectors and selected streamlines: the orifice flow (A), the jet shear layer (B), the impingement on the cube and the bottom wall (C), the separation and the reattachment regions around the cube (D), the wakes behind the cube and the jet (E) and the recirculation bubble in front of the cube (F). Although there is a strong interaction between the zones, one can identify major features of each phenomenon and their effects on the thermal field.

The relatively smooth streamline patterns in Fig. 4b conceal the complex and unsteady vortex morphology which develops in multiple shear layers around the jet and the cube. This is illustrated in

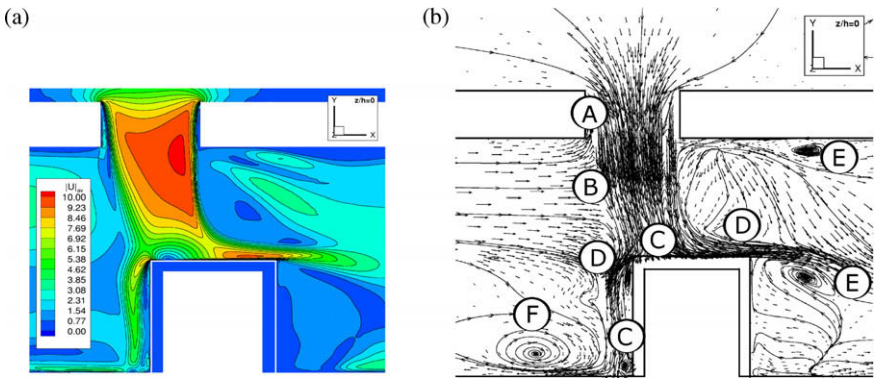

Fig. 4. Contour plots of the average velocity magnitude (a) and identification of the characteristic flow zones (b) in the vertical midplane $z/h = 0$ (left).

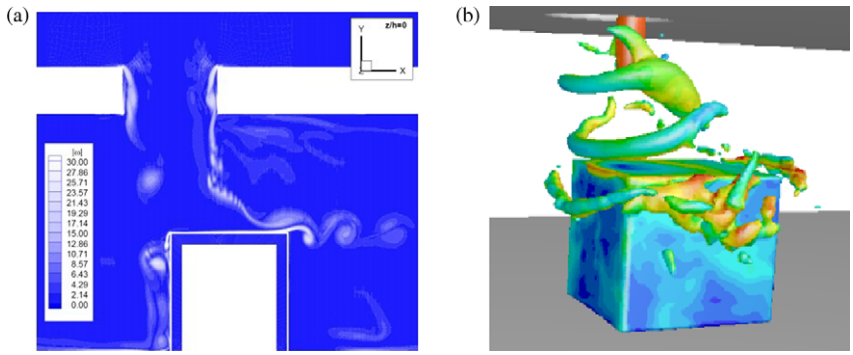

Fig. 5. Snapshots of the instantaneous vorticity magnitude in the vertical midplane (a) and of the vortex ring structure (b); the latter is identified by the pressure isosurfaces and coloured with the velocity magnitude.

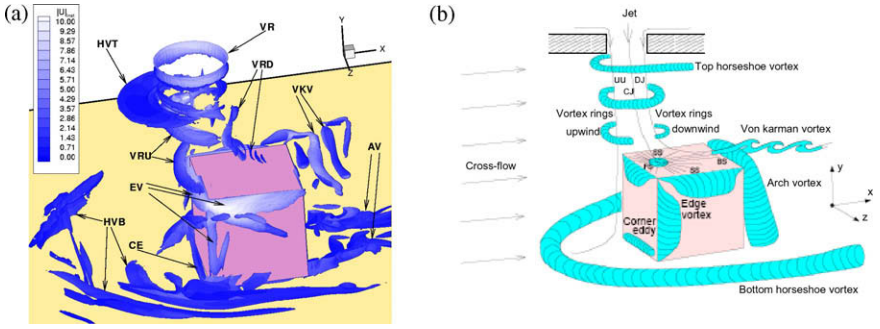

Fig. 6. Flow structures around the cube identified by the isosurfaces of Q shaded with the instantaneous velocity magnitude (a) and "artist impression" of the vortex morphology (b).

Fig. 5a by an instantaneous snapshot of the vorticity magnitude in the same vertical midplane, showing several vortex systems. Despite steady conditions, the flow was found to be inherently unsteady with periodic formation of ring vortices in the jet shear layer. This is illustrated by a snapshot of coherent structures identified by the constant-pressure surfaces in Fig. 5b, showing a typical sequence of vortical rings around the jet, being subsequently deformed and swept by the crossflow.

The full three-dimensional picture is even more complex, as illustrated in Fig. 6a, where the vortical structures have been identified by the Q parameter, defined as $Q = 1/2(|\Omega|^2 - |S|^2)$, where $|\Omega| = \Omega_{ij}\,\Omega_{ji}$ and $|S| = S_{ij}S_{ji}$, and Ω_{ij} is the vorticity and S_{ij} is the rate-of-strain tensor. An *a posteriori* drawn sketch in Fig. 6b summarizes the most conspicuous vortex systems, providing also explanation of the acronyms used in Fig. 6a for their identification. We consider now in more details specific features of vortex morphology in each of the characteristic zones.

3.1.1. The flow in the orifice and formation of the jet and ring vortices

In the setup here considered, the jet is formed from the flow in the top chamber that passes through the orifice in its bottom wall. Since the flow at the entrance of the orifice is not directed perfectly in the radial direction, there is a velocity component tangential to the orifice that will cause the rotation of the fluid in the orifice in one direction or another, depending on the initial instabilities. This creates a swirling motion of the jet that extends along the core of the jet all the way to the top face of the cube, as shown on Fig. 7a. It can be seen both from the velocity vector plot and the contour plot that the centre of the rotation is slightly shifted from the centreline of the orifice in the direction of the oncoming flow from the top chamber (positive x-direction). From the pathlines given in Fig. 7a it is clear that the swirling is intensive only within the core in the central region of the jet.

The swirling motion is restricted to the jet core region, because there the angular momentum has very little resistance apart from the viscous forces at the edges. Outside of the core of the jet, however, the swirling motion does not survive very long, because it is surrounded by the shear layer where the intensive mixing is taking place due to the entrainment and vortex pairing. It was also found (not shown here) that the central high vorticity region (core of the jet) remains its position over the whole length of the jet. On the other hand, the outer vortex rings keep their original identity only shortly, just after the orifice, and further downstream they get deformed in the interaction with the crossflow.

Because of the orifice sharp edges, the Kelvin–Helmholtz instabilities appear already within the orifice. An asymmetric ring-shaped separation bubble is created, especially visible in the upstream side of the orifice, Popovac [9], which trigger periodic generation of roll-up vortex rings in the jet shear layer, seen in Fig. 5b and denoted as *VR* in Fig. 6a. The centres of the vortex rings are characterised by the local low pressure, which is clearly seen from the instantaneous vorticity field given in Fig. 5a. These large-scale strong structures dominate the local flow dynamics, the mixing process and the cooling of the cube.

The generation of the vortex rings around the jet is related to intensive shearing in the jet shear layer, which in the present case is intensified by the interaction with the lateral crossflow. The peaks in the profiles of the uv turbulent stress component above the top face of the central cube, [9], reflects well this high shearing activity in the outer region of the jet. Due to differences in the flow conditions around the jet, the vortex rings are not symmetrical, hence in Fig. 6 the upstream vortex ring is denoted as *VRU* and the downwind one as *VRD*. On the upstream side the evolution of the shear layer vortices *VRU* is very distinct, whereas on the downstream side vortices *VRD* break up easier due to the jet bending. This is clearly shown in Fig. 5b: initially the vortex rings stay

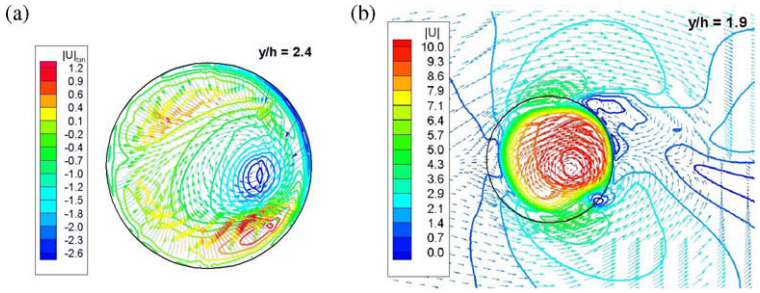

Fig. 7. Velocity field in a cross-section in of the orifice (a) and in and around the jet just after its exit from the orifice (b).

parallel to the orifice edge, but as they travel along with the jet these vortex rings get tilted following the deflection of the jet. On the downwind side of the jet the rings are breaking up faster, while the upwind ones retain their identity and disperse only after hitting the surface of the cube.

3.1.2. The jet

The most prominent feature of a jet in a crossflow is the jet deflection due to the pressure exerted by the lateral flow. A pressure drop develops around the jet in the crossflow direction, which creates a recirculation zone behind it just as in flows around bluff bodies. The intensity of this effect depends on the velocity ratio α_v, which governs the interaction of the two streams and their mixing in the jet periphery, Rivero et al. [11]. Due to collision of the two mutually perpendicular streams and the shear-driven entrainment, the jet begins to acquire a characteristic kidney shape. Furthermore, in the present case the deflection is intensified by the *vena contracta* of the jet cross-section (Fig. 4b).

The horseshoe vortex formed around the jet at the orifice exit, denoted as *HVT* in Fig. 6a, is similar to that found in a cylinder-wall (or a wing-body) junction flows. The important difference is, however, that in a flow over solid-bodies junction there are mechanical obstacles. In the present case, as shown in Fig. 6a, there is a "gap" between the jet and the lower edge of the orifice at the top wall of the channel, through which the lateral flow enters into the orifice. This is the main difference in the dynamics between the horseshoe vortex in junction flows and *HVT* in the present case. While in junction flows there is an unsteady horseshoe vortex formation around the cylinder that depends on one side on the geometrical parameters such as the diameter of the cylinder and the boundary layer thickness and characteristics of the oncoming flow on the other (Simpson [12]), in the present case the horseshoe dynamics is entirely dictated by the dynamics of the jet shear layer roll-up vortices *VR*, Fig. 6a, which are already initiated on the upper edge of the orifice at the bottom wall of the plenum chamber.

Related to the formation of *HVT* is the creation of the recirculation zone on the downwind side of the jet. Fig. 7b illustrates how this horseshoe vortex wraps around the jet, separates and recirculates behind it. The centre of the recirculation bubble, which is denoted as *RB* in Fig. 8 below, is at $x_{RB}/h = 0.49$.

The core of the jet, where the velocity remains relatively unaffected, is surrounded by the growing mixing layer. As the mixing layer grows, the core shrinks until it completely vanishes when the mixing layer reaches the centreline of the jet. Patte and Baines

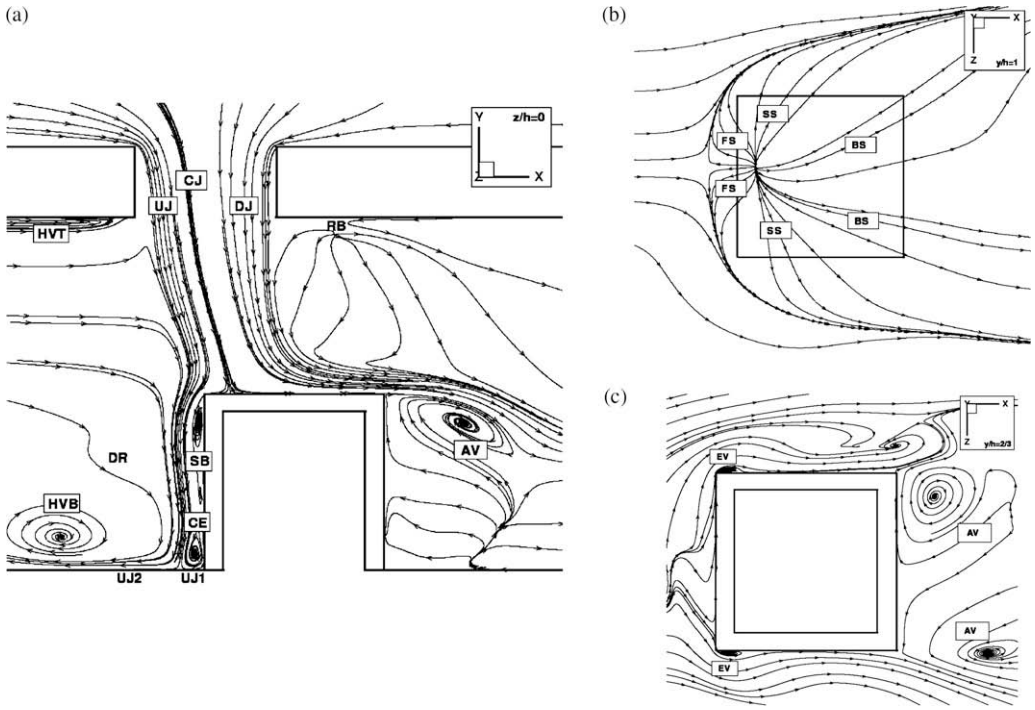

Fig. 8. Notation of the main recirculation bubbles ("vortices") and identification of the characteristic time-averaged streamlines in the vertical midplane $z/h = 0$ (*a*), and in the horizontal cutplanes at $y/h = 1.0$ (b) and $y/h = 0.66$ (c).

[13] concluded that for a jet in a crossflow the core of the jet extends up to $y/D = \alpha_v$. In the present case the top face of the cube, at $y/D = 1.25$, falls within the core region. The instabilities in the jet shear layer continue to generate vortex rings (already initiated in the orifice), which are advected with the jet. The low pressure zones, such as those shown in Fig. 5a, indicate the centres of these vortices. In a free jet the vortex rings are losing their phase lock and the structure coherence as they travel further away, whereas for the jet in a crossflow this effect is intensified due to the different flow conditions around the jet (the difference in the pressure on the upstream and downstream side of the jet).

A closer look at the average streamline patterns in the vertical midplane and in two horizontal planes, at the cube top ($y/h = 1.0$) and at the half cube height, is presented in Fig. 8. In order to facilitate the analysis of the flow morphology and heat transfer, Fig. 8 provides notations assigned to the most conspicuous vortex systems, identified already in Fig. 6, and to several characteristic sets of streamlines. The latter are denoted as the upstream, central and downstream jet streamlines, *UJ, CJ and DJ* respectively. The upwind part of the jet *UJ*, first slightly deflected in the streamwise direction by the crossflow, hits the cube top leading edge and then bends upstream creating a separation bubble (*SB*) at the upper part of the front face. The stream reattaches on the front face and impinges subsequently on the bottom channel wall, creating another separation bubble (corner eddy, *CE*) at the foot of the front face encompassing a part of fluid (*DJ1*), whereas the bulk fluid flows back and gets entrained into a strong bottom horseshow vortex (*HVB*) in front of the cube. The downwind part of the jet, denoted by *DJ*, impinges on the cube and slides over the top face downstream and towards the cube sides, creating a wall boundary layer. After separation at the top leeward edge, fluid leaves the cube surface in form of a strong plane free shear layer, which creates a vortex street and a massive separation behind the cube. An asymmetric arch vortex (*AV*) is formed, with its legs mutually displaced in the streamwise direction, as seen in Fig. 8c. The lateral (channel) flow separates on the side edges creating small separation bubbles at each side (*EV*). The flow reattaches and forms boundary layers on side faces, separate at their leeward edges, to be partially entrained into the arch vortex, whereas the outer bulk of the fluid flows downstream. The vortex rings *VRU* and *VRD* (Fig. 8a) are the strongest coherent structures with characteristic shedding frequency $St = 0.81$, where the Strouhal number St is based on the orifice diameter D and the jet bulk velocity U_j. Being advected by the jet, the vortex rings *VRU* and *VRD* break up on the cube top surface, followed by a developing boundary layer.

From the experimental investigation of a circular jet in a crossflow at various Reynolds numbers Patte and Baines [13] derived an empirical expression for the "shape" streamlines of the jet in the far-field for different velocity ratios α_v

$$\frac{y_i}{D\alpha_v} = C_i\left(\frac{x}{D\alpha_v}\right)^{0.28}$$

The subscript "*i*" refers to the upwind, the centreline and the downwind shape streamline (denoted respectively by "u", "c" and "d") of the jet, Fig. 6d, x is the coordinate in the direction of the lateral flow, y is the coordinate in the direction of the issuing of the jet, and the origin of the coordinate system is placed in the centre of the jet exit. The coefficient C_i takes the value 2.36, 2.05 and 1.35 for the upstream, the centreline and the downstream streamline respectively.

In the present case the jet deflection, calculated from the location of the impingement point at the top face of *C3* reads $x_c/D = 0.18$ as compared with the experimental value $(x_c/D)_{\exp} = 0.15$ found for the similar flow conditions by Muppidi and Mahesh [14]. The difference in the predictions can be attributed to the difference in the flow setup: the experiments are performed with the jet issued from a straight pipe, whereas here the jet issues from the plenum chamber through an orifice.

3.1.3. Vortex structures around the cube

Unlike the events taking place around the jet, the flow structures around the cube are wall-related. We consider now the vortex morphology in the vicinity of each cube side.

Front face. As shown in Fig. 8, the downwind and the centreline jet streamlines, empirically predicted by Eq. (1.1), hit the cube. However, the velocity ratio α_v is relatively low so the upwind streamlines of the jet do not reach the leading edge of the cube. Therefore, only the central and the downwind part of the jet, *CJ* and *DJ* respectively, impinge onto the top cube face. The upwind part *UJ*, with a smaller momentum, passes in front of the cube leading edge. Being largely protected from the influence of the lateral flow by the upwind cube *C2*, *UJ* impinges onto the bottom wall of the channel at $x_{I2}/h = -0.15$.

The fact that the upwind part of the jet *UJ* passes in front of the cube influences significantly the overall cooling of the cube, making it spatially more uniform. When *UJ* impinges onto the bottom of the channel, it splits into two parts. The streamlines *UJ1* go towards the central cube, and creates the corner eddy denoted as *CE* in Fig. 8. This recirculation bubble extends $y_{CE}/h = 0.23$ up the cube. In the centre of *CE* the turbulent shear stress component *vw* reaches its peak values [2].

The streamlines *UJ2* flow in the opposite direction, towards *C2*, to merge with the horseshoe vortex which is located at $x_{HVB}/h = -1.18$ in front of the cube *C3*. This horseshoe vortex, denoted as *HVB* in Fig. 6, is created between the central heated cube *C3* and the upstream cube *C2*, since the centre-to-centre distance $d = 4h$ is sufficient to accommodate the flow structure that wraps around the *C3* cube. The profiles of the velocity magnitude just above the bottom wall, given in Fig. 9, depict the flow pattern of the horseshoe vortex *HVB*. After the corner eddy *CE* the bottom *HVB* extends up to the saddle point. The set of these saddle points (shifted for different cutlines in Fig. 9) create the separation line between the horseshoe vortex and the secondary vortex.

Top face. The downwind and the centreline jet streamlines *DJ* and *CJ*, which impinge onto the cube top face at $x_{I1}/h = 0.15$, spread over the face and flow towards the edges where the separation takes place, as indicated in Fig. 8b. The front streamlines *FS* flow over the leading edge in the region, denoted as *DR*, and deflect the lateral flow and the upwind streamline of the jet *UJ*. Passing the leading edge, *FS* streamlines create a separation bubble on the front cube side, of the size $y_{SB}/h = 0.39$. On the trailing edge

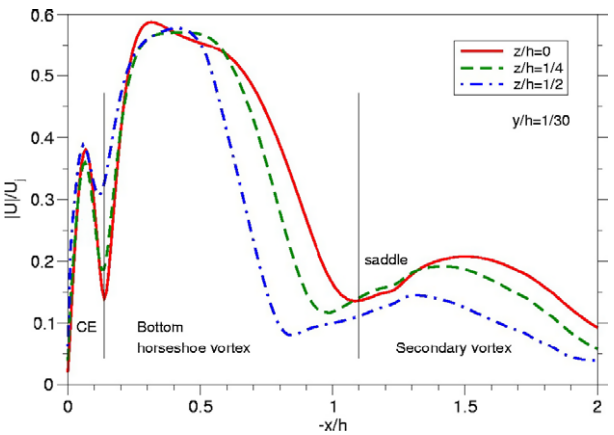

Fig. 9. Profiles of the velocity magnitude along the cutlines above the bottom wall in the cutplane $y/h = 0.03$.

of the top face the back streamlines *BS* indicate a massive separation of the lateral bulk flow that takes place behind the cube. In fact, two sets of streamlines flowing towards the trailing edge of *C3* can be identified, with high shear between the two: the part of the fluid escaping from the impingement region, and the part coming from the jet's downwind shear layer together with its characteristic vortex rings. This flow situation causes the creation of the von Karman vortices, as discussed below.

The location of the impingement point *I1* is fixed only in the averaged sense. The instantaneous positions of the impingement point are in fact shifting along the spanwise direction. Another interesting feature of the instantaneous impingements is that it occasionally splits in two. A series of snapshots of the instantaneous velocity magnitude contours (see in Popovac [9]) just above the top face of the cube show the unsteady nature of the impingement zone.

Side face. The separation of the side streamlines *SS* on the cube side edges of the top face interact with the lateral bulk flow. One set of these new streamlines stay attached to the side faces, while the other bends away from the cube. On the upper front corner of the cube the edge vortex *EV* is created, as seen in Fig. 8b, resulting from the interaction between the impinging jet and the lateral crossflow, and it is confined by the cube and the bulk stream of the lateral channel flow. It plays an important role in enhancing cooling of the cube, especially on its side faces.

Back face. Behind the back face of the central cube a large arch vortex is created, with the centre located at $x_{AV}/h = 1.49$. The imprint of this vortex at the bottom wall is marked with *AV* in Fig. 6. The dominant fluctuation in this region is in the spanwise direction, as confirmed by the profiles of the *uu* and *uw* turbulent stress components behind the cube (Popovac [9]).

The vortex rings from the jet's downwind side *VRD* are being advected by the jet, and as they reach the cube *C3*, they slide over its top face. Hence, towards the trailing edge of the top face the boundary layer that is developing from the fluid leaving the impingement zone *I1* is being subjected to the local adverse pressure gradient, generated by the vortex ring *VRD* hitting the top face. This initiates the boundary layer to separate creating the von Karman vortex street *VKV* behind the cube, as already seen in Fig. 5.

The appearance of the von Karman vortex street is associated with high gradients of the mean velocities, which contribute to high production of the turbulent stresses. This is the region of high intensity of the *uu* Reynolds stress component, particularly visible at the trailing edge of the back face of the cube (Popovac [9]).

3.1.4. Spectra and the characteristic frequencies

The spectra of the power density *E* of the velocity signal taken at the four characteristic monitoring points are shown in Fig. 10. In the jet shear layer, Fig. 10a and b, show the natural frequency of the occurrence of the roll-up vortex rings. The frequency of these structures f_s is given in terms of the Strouhal number $St_s = f_s D/U_j$. For the *VRU* roll-up vortex rings on the upwind side of the jet the peak of the spectrum (the first mode) is at $St_{VRU} = 0.81$, Fig. 10a. For the vortex on the downwind side *VRD* the spectral peak is not so pronounced, yet the same value $St_{VRD} = 0.81$ can be identified, Fig. 10b. It is obvious from Fig. 10a and b that these vortical structures are very strong at the upwind side of the jet, while on

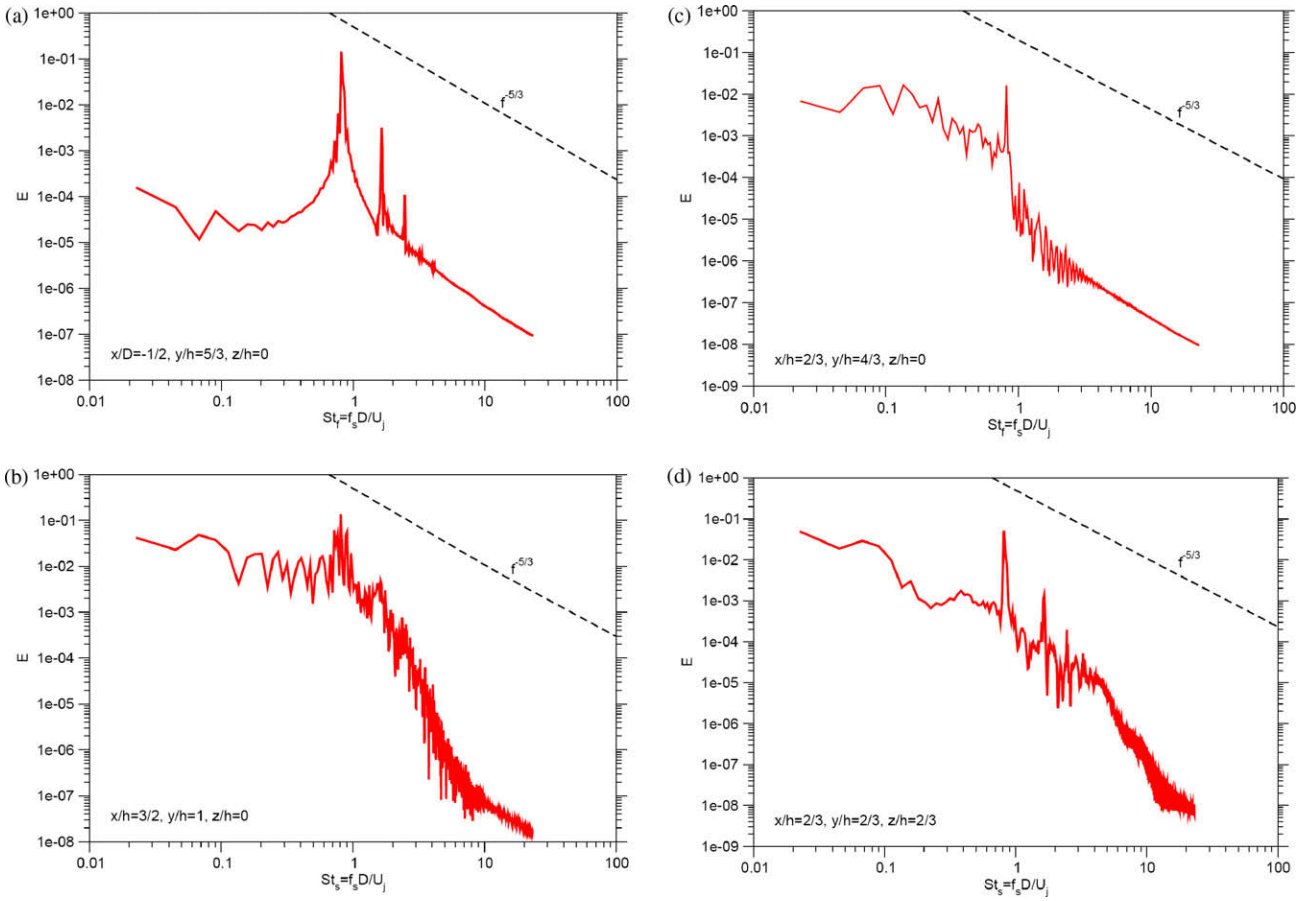

Fig. 10. Power spectra in terms of Strouhal number at characteristic monitoring points: (a) in the upwind *VRU* and (b) downwind region *VRD* of the jet shear layer; (c) behind the cube, *VKV* and (d) on the side of the cube.

the downwind side they break up faster. The power density spectrum of the velocity signal taken at the side of the cube, gives the Strouhal number of the edge vortex characteristic frequency $St_{EV} = 0.81$, which is the same as the frequency of the roll-up vortex rings. Obviously the vortex rings which are breaking on the top face of the cube act as a forcing for the edge vortex created at the corner of that face.

It is only natural to expect that vortices in the Von Karman street behind the cube, *VKV*, will have the same frequency as the vortex rings which are initiating that process. As seen in Fig. 10c and d, the power density spectra obtained from the velocity signal at a point behind the cube confirmed this expectation, giving $St_{VKV} = 0.81$.

Two additional checks have been done in order to verify the characteristic Strouhal number identified on the power density spectra. From a sequence of snapshots of the vortex rings along the jet, the period of their occurrence was evaluated and found to give approximately the obtained value of the Strouhal number. The obtained frequency can be deduced also from the distance between the rings ($0.4\,h$) and their averaged advection velocity. Looking at the self-similar solution for the axial velocity component of the free jet (Rajaratnam [15]), a realistic value for that position would be approximately one half of jet's centreline velocity ≈ 4 m/s.

The obtained value of the Strouhal number is somewhat higher than those reported in the literature for the single impinging jet, but this is explained by the influence of the crossflow and the vicinity of the impingement cube top surface. The formation of the vortex ripples, and hence the Strouhal number of the vortex rings, is highly sensitive to the flow conditions of the surrounding fluid. Gutmark and Ho [16] showed that even very small coherent disturbances, up to $\mathcal{O}(5 \times 10^{-5} U_{ref})$, can have appreciable effect on the vortex ripple formation. In the present case the crossflow stream penetrates into the orifice, creating a recirculation zone there, and triggers the instability of te Kelvin–Helmholtz type. This two-way coupling between the recirculating fluid inside the orifice and the oncoming jet, discernible from the instantaneous pathlines in Fig. 4b (for further illustrations see [9]) is the dominant effect that determines the frequency of the vortex rings. Thus the frequency of the vortex rings is the frequency of the interaction between the jet and the crossflow.

3.2. Thermal field and turbulent heat flux

3.2.1. Surface temperature and heat flux

The averaged temperature field on the cube faces is presented in Fig. 11, showing the contours of the temperature difference $\Delta\Theta_{av}$ between the average surface temperature Θ_s and the fluid inflow temperature Θ_{in}. As expected, the temperature contours on the cube surface follow closely the flow and vortical patterns established around the cube. Namely, the temperature of the top face shows almost a uniform distribution, apart from edges, because it is almost entirely washed by the impinging jet. On the front face, the recirculation zones established by the corner eddy *CE* at the bottom and the edge vortex *EV* at the top are characterised by an increase in the temperature relative to the rest of the face. The heat removal on the side face is influenced by the flush of the fresh air that extends rather diagonally across the face. The zone of an increased temperature on the back face of the cube follows the legs of the arch vortex *AV* established behind the cube.

A quantitative comparison between the (normalised) measured and simulated temperature distributions along the centrelines in the vertical and horizontal midplanes has been presented and discussed in Popovac and Hanjalić [2], showing good agreement with the experiments of Tummers et al. [1] over the most portions of the cutlines. Discrepancies were found only around the bottom parts of the front and back face, attributed to the difference in the treatment of the junction between the bottom wall and the central cube, and to a small difference between the experimental and computational jet displacement, discussed earlier.

The snapshots of the instantaneous temperature on the cube surface shown at two time instants corresponding to the same phase angle of the characteristic period of vortex shedding (corresponding to St = 0.81) in Fig. 12a and b, viewed from behind, look both similar to the averaged temperature shown in Fig. 11. The pattern changes with time and should reflect the velocity fluctuations close to the cube surface. However, because of low conductivity, very small thickness of the epoxy layer and the constant temperature imposed by the copper core on the interior epoxy surface, as well as very intensive cooling, the temperature fluctuations are damped and show even a small phase lag. For comparison, a snapshot of the same cube but without a jet from Ničeno et al. [3], Fig. 12c, shows much more vigour and nonuniformity due to the absence of the dominant jet impingement. Here the effects of the local vortical structures around the cube side- and leeward faces are much more pronounced.

For the functionality of electronic components the occurrence of *hot spots* is as dangerous as the high temperatures themselves. The hot spots are the isolated regions of high temperature, and they cause high thermal stresses in solids. Especially critical could be the unsteady thermal stresses that cause a thermal fatigue of the material. The unsteadiness of the thermal stress is caused by the time migration of hot spots in solids, induced by the unsteady local vortical structures and their imprints on the surface. Hence, for a good cooling of electronic devices, the removal of heat has to be efficient but also uniform over all faces of the components. The hot spots on the cube surface can be seen in Fig. 12. They are visible especially on the back face of the cube, where the velocity is much lower due to recirculation of the fluid trapped in the multiple recirculation bubbles. However, the comparison of the instantaneous temperature distributions in the present simulations with those of Ničeno et al. [3] in a similar configuration (cubes in a matrix) but without a jet, show generally more uniform temperature distribution and less pronounced and fewer hot spots due to the strong

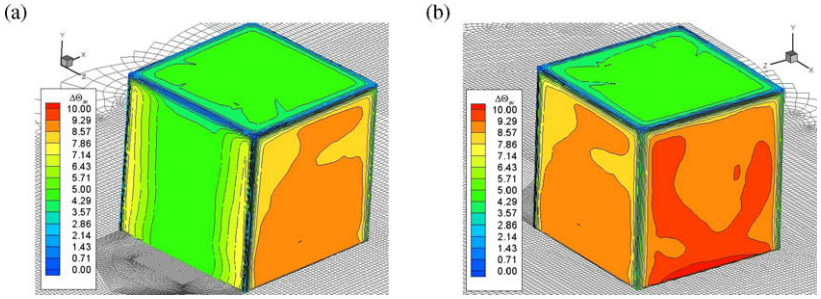

Fig. 11. Contours of the averaged temperature (relative to the fluid inflow temperature) on the surface of the heated cube. (a) view from the front, (b) view from back.

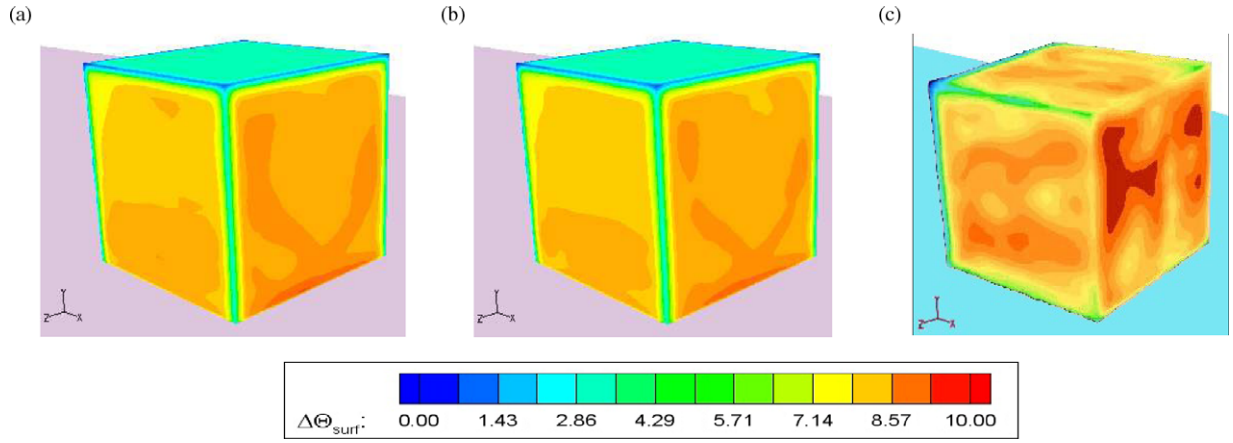

Fig. 12. (a) and (b): snapshots of the instantaneous temperature on the cube surface at the same phase angle in two cycles, t_0 and $t_0 + 2\tau$, where τ is the period of the vortex systems (for St = 0.81). The colour bar denotes $\Delta\Theta_{surf}$ [C]. (c): a snapshot of the surface temperature without jet, [3].

cooling effect of the impinging jet and its turbulizing effects on the flow along the cube side- and leeward faces.

The surface temperature reflects heat transfer, but a better indication of the mechanisms that remove heat and their relation to the fluid velocity field can be drawn from information of the surface heat flux. The classic way of relating the surface heat flux with the friction, as implied by the Reynolds analogy (though relevant only to attached wall flows), obviously fails in the present situation, as illustrated in Fig. 13a and b: not much similarity could be drawn between the two wall phenomena, except perhaps on the top face. However, the comparison with the pressure field showed more resemblance, especially on the front and side surfaces, Fig. 13b and c. This was also found experimentally by Meinders [17] for flows in a matrix of the same cube arrangement but without a jet, who argued that the velocity–pressure coupling through the momentum equation, and the velocity–temperature dependence in the energy equation, brings in a similarity between the latter two fields. Indeed, Meinders [17] reported a similarity between the relative average pressure and the relative average heat flux on the same surface. The explanation could be found in the effect of the impinging crossflow and jet, which both create a high pressure in and around the stagnation zones, with high velocities of the fluid spreading away from it, thus enhancing also the heat flux. One would expect that the friction coefficient behaves in a similar manner, but its distribution shown in Fig. 13a is more nonuniform. It is obvious that the relative average heat flux (the ratio between the local heat flux and the surface averaged heat flux) is higher in the impingement zones and in the edge vortex region.

The thermal plumes created around and behind the cube give a qualitative image of the three-dimensional temperature field and the underlying vortical structures. The isosurface of the instantaneous temperature of the fluid coloured with the contour plot of the velocity magnitude, Fig. 14, depict the flow structures that contribute most to the heat removal from the cube surface. Around the cube faces that are well cooled, this isosurface is very close to the cube. On the other hand, the separation zones created around all the cube edges extend the isosurface further in the domain. The nonuniform heat removal across the face is characterised by a strong time-meandering of the plume surface, seen especially on the rear face of the cube.

As discussed above, the highest temperatures on the cube surface are obtained at the bottom of the rear face, because this is the region of very low velocities. There the recirculation is established, hence the velocities are low, and due to weak heat removal the surface temperature gets high. Tummers et al. [1] anticipated that buoyancy could be important in this region, but found it to be negligible as compared to inertial forces. Therefore, buoyancy effects have not been accounted for in the present simulations. However, due to high temperatures and low velocities in this region, a link between the local flow structures and the thermal field can be clearly recognized. This is illustrated in Fig. 15 showing blowups of the velocity vectors and the temperature isolines in the bottom corners of the front and the back face in the vertical midplane $z/h = 0$. The eddies are thinning the thermal boundary layer, but they are also convecting away the hot fluid from the surface and creating small thermal plumes. This is confirmed by the velocity vectors further away from the cube surfaces, which are

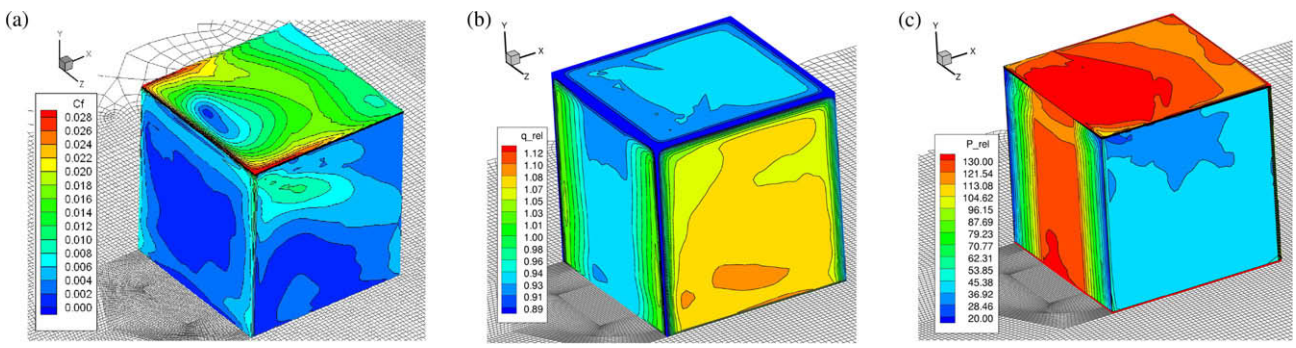

Fig. 13. Contours of the averaged friction factor (a) nondimensional heat flux (b) and relative pressure (c) on the surface of the central cube.

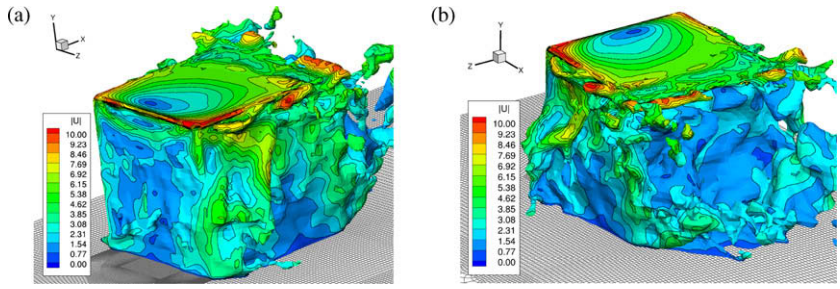

Fig. 14. A selected temperature isosurface coloured with the velocity magnitude: the front side view (a) and the back side view (b).

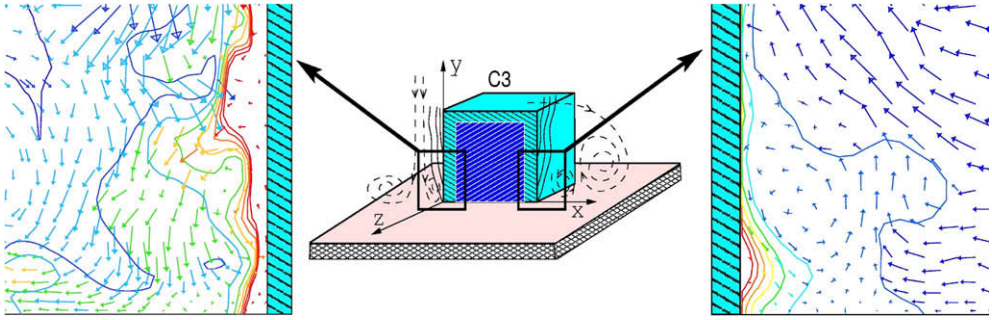

Fig. 15. Temperature contour lines and the vector plot in the vertical midplane $z/h = 0$ in the wall vicinity indicate the correlation between the thermal and the velocity field: the bottom corner in front of (left) and behind (right) the central cube.

more or less oriented in the direction normal to the temperature isocontours.

3.2.2. Turbulent heat fluxes

The best indicator of the thermal activity in the flow is the turbulent heat flux vector. Since the temperature was treated as a passive scalar in this computation, one can expect a relation between the turbulent momentum fluxes (the Reynolds stresses) and the turbulent heat fluxes. A qualitative comparison is presented in the figures that follow showing contour of corresponding turbulent stress and flux components in the vertical midplane $z/h = 0$ and the horizontal cutplane $y/h = 0.66$ (only half is shown due to assumed symmetry). Fig. 16 compares the $u\theta$ with the uu and uv stress components, whereas Figs. 17 and 18 show the $v\theta$ versus vv, and $w\theta$

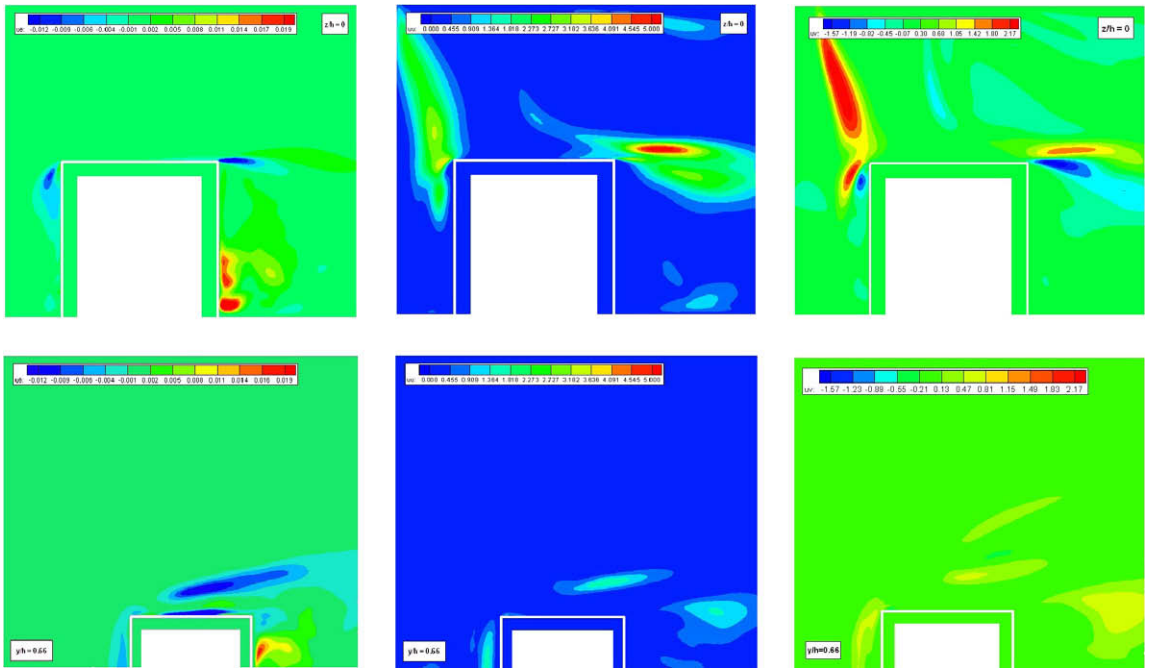

Fig. 16. Qualitative comparison between the $u\theta$ turbulent heat flux (left), the uu (middle) and the uv turbulent stress (right), in the cutplanes $z/h = 0$ (top) and $y/h = 0.66$ (bottom).

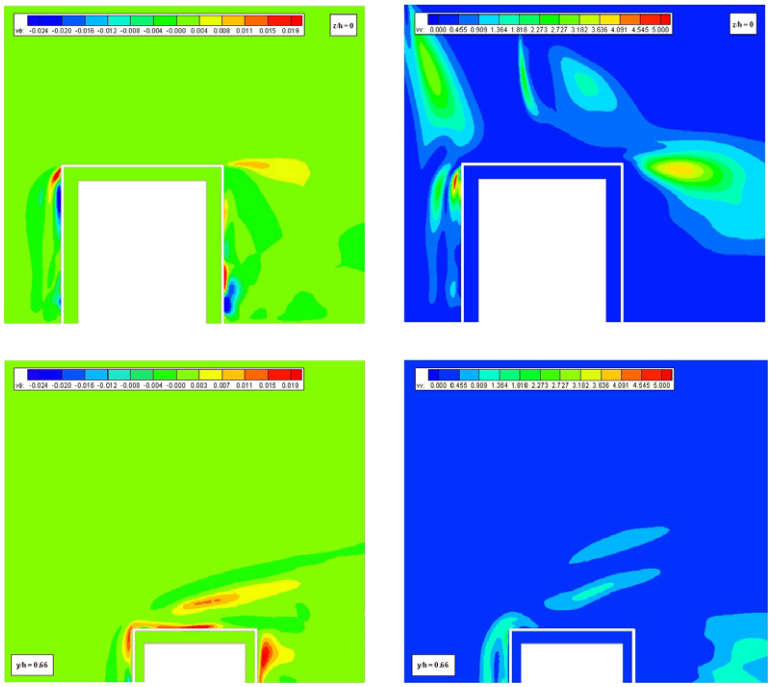

Fig. 17. Qualitative comparison between the $v\theta$ turbulent heat flux (left) and the vv turbulent stress (right), in the cutplanes $z/h = 0$ (top) and $y/h = 0.66$ (bottom).

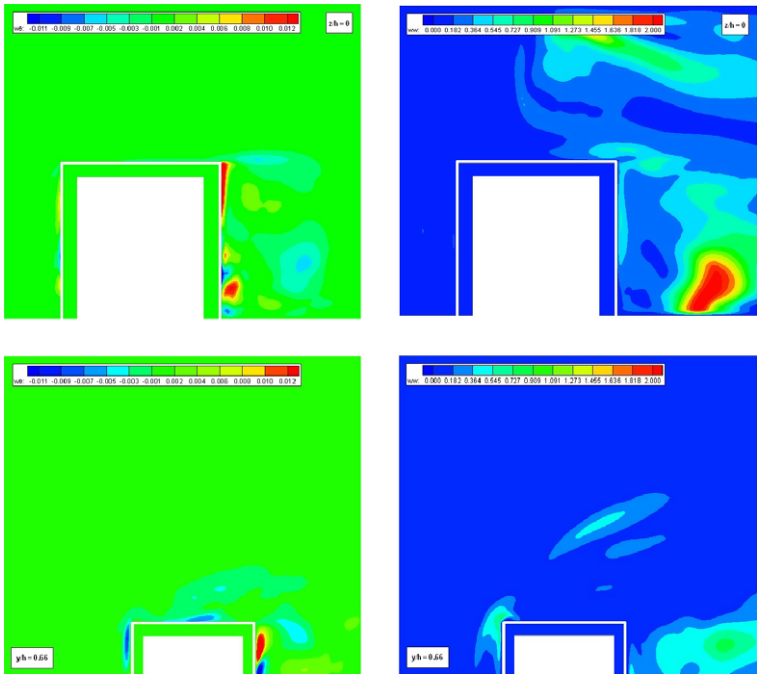

Fig. 18. Qualitative comparison between the $w\theta$ turbulent heat flux (left) and the ww turbulent stress (right), in the cutplanes $z/h = 0$ (top) and $y/h = 0.66$ (bottom).

versus ww, respectively. It is clear that the highest intensities of the turbulent heat flux components occur in the regions of high turbulent stresses associated either with a strong shear, or with the large vortical structures: the edge vortex *EV* on the side faces of the cube, the Von Karman vortex street *VKV* and the arc vortex *AV* behind the cube, and the corner eddy *CE* and the separation bubble *SB* on the front side of the cube.

The impingement zone extends over almost the entire top face of the central cube. This is a very efficient heat removal mechanism, and therefore the top face of the cube is very well cooled. The edge vortex *EV* constantly brings fresh fluid of the lateral stream in the near-wall zone of the side face, which would otherwise be covered by the recirculation bubble and hence much less efficiently cooled. Flowing over the side edges of this face, the lateral flow creates the separation bubble *SB* at these edges close to the bottom wall. Therefore, apart from the lower front corner, the rest of the side faces are very well cooled.

The upwind part of the jet passes along the front cube face, washing it with a fresh fluid which ensures high heat transfer rate. Only at the bottom of the front face, where the corner eddy *CE* is

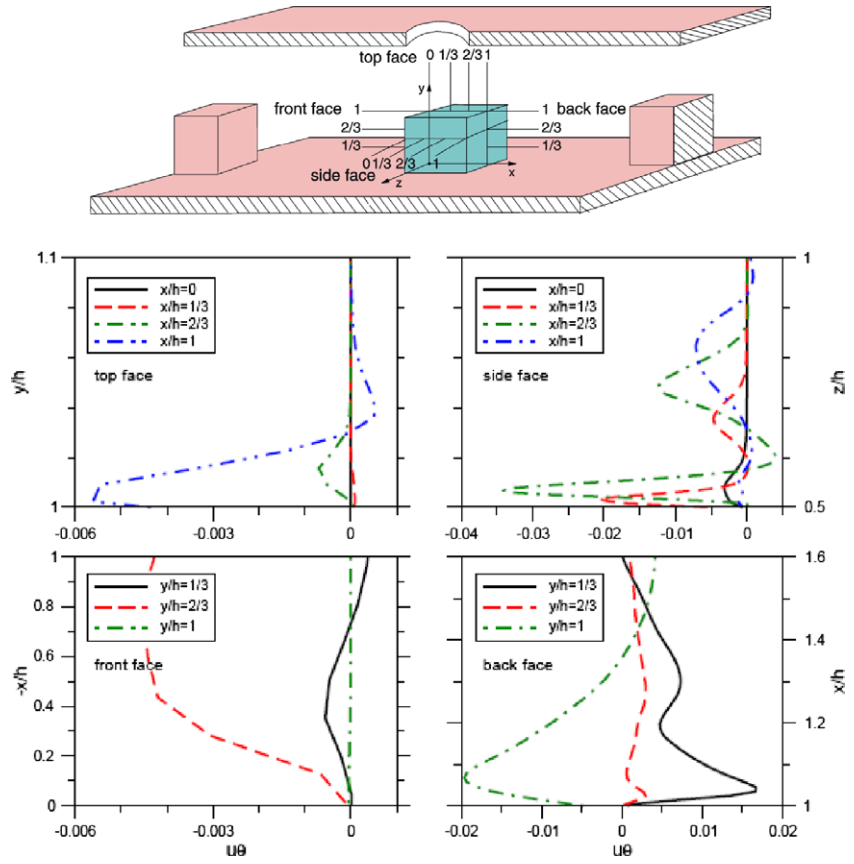

Fig. 19. Profiles of the $u\theta$ turbulent heat flux component around the cube *C3* (plotted in the appropriate direction starting from the surface of the cube) in the cuplanes $z/h = 0$ and $y/h = 0.66$.

created, the cooling is somewhat reduced. The back face of the cube is its least cooled part. Due to the recirculation created behind the cube, the hot fluid stays trapped in that region and the heat transfer becomes poor. For that reason two vertical stripes of high temperature following the legs of the arc vortex *AV* formed behind the cube. Only the side edges of the back face have relatively lower temperature where the arc vortex entrains the fresh fluid from the lateral flow towards the recirculation region.

The quantitative illustrations are provided in Figs. 19–21, showing the profiles of the turbulent heat fluxes, $u\theta$, $v\theta$, and $w\theta$ respectively, at several cutlines in all directions around the central heated cube *C3* .

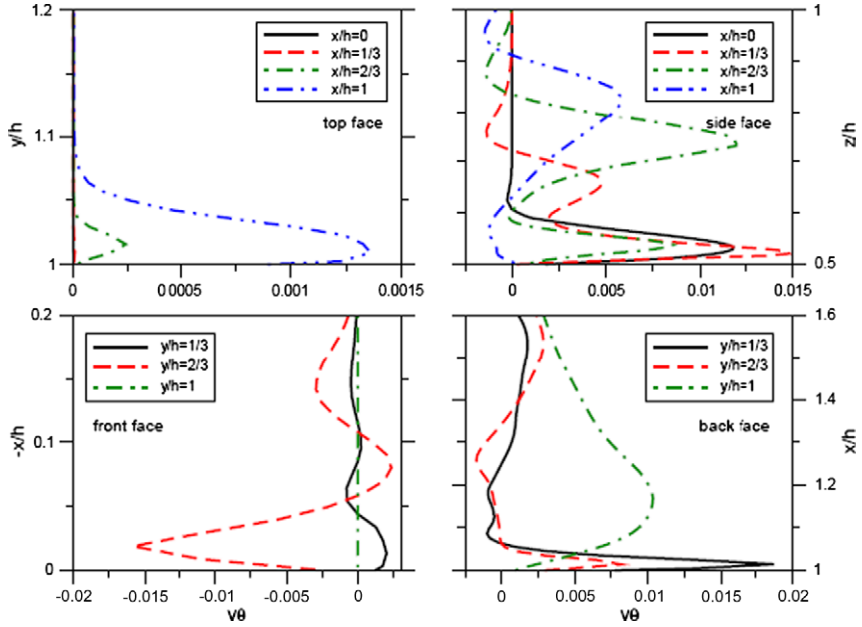

Fig. 20. Profiles of the $v\theta$ turbulent heat flux component around the cube *C3* (plotted in the appropriate direction starting from the surface of the cube) in the cuplanes $z/h = 0$ and $y/h = 0.66$.

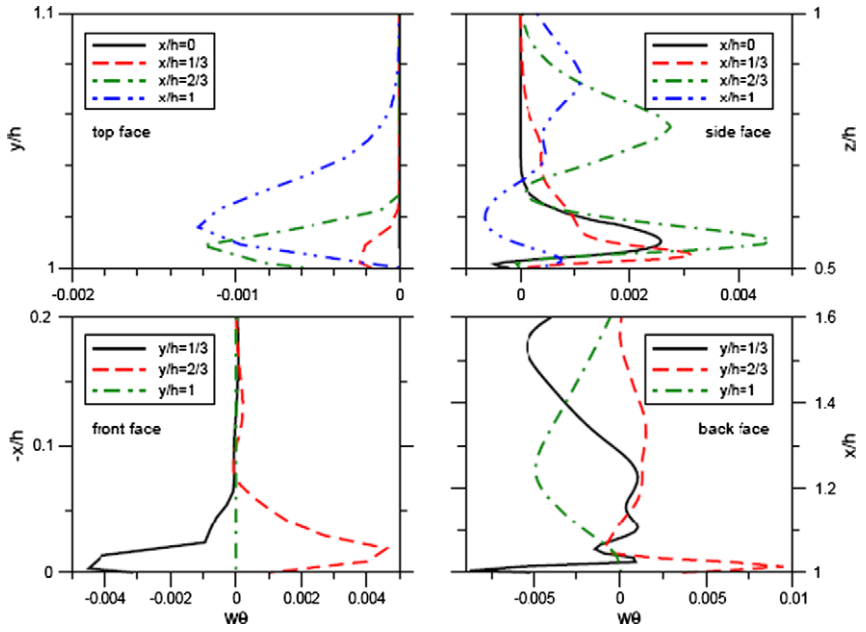

Fig. 21. Profiles of the $w\theta$ turbulent heat flux component around the cube *C3* (plotted in the appropriate direction starting from the surface of the cube) in the cuplanes $z/h = 0$ and $y/h = 0.66$.

3.2.3. Budgets of the turbulent heat flux

The dynamics of the turbulent heat flux is best illustrated by its "budget" i.e. distribution of various terms in the differential transport equation governing the flux. A detailed analysis of the budgets for all three flux components and their comparison with the budget of corresponding stress components can be found in Popovac [9]. Here, as an illustration, Fig. 22 shows the profiles of the $u\theta$ and $w\theta$ budget terms in the cutlines along the x-direction in front and behind the central cube *C3* respectively.

In order to describe the overall heat transfer mechanism, let us follow selected imaginary pathlines around the central cube *C3*. When the jet impinges onto the top face of the cube the mean velocity tends to zero, hence the convection is negligible. The dominant effect for the heat transport in that region is represented by the temperature-pressure gradient (pressure-scrambling) term, while the production of the normal turbulent stresses becomes negative. After the impingement, the fluid that escapes from the impingement region flows over the leading edge of the cube, where

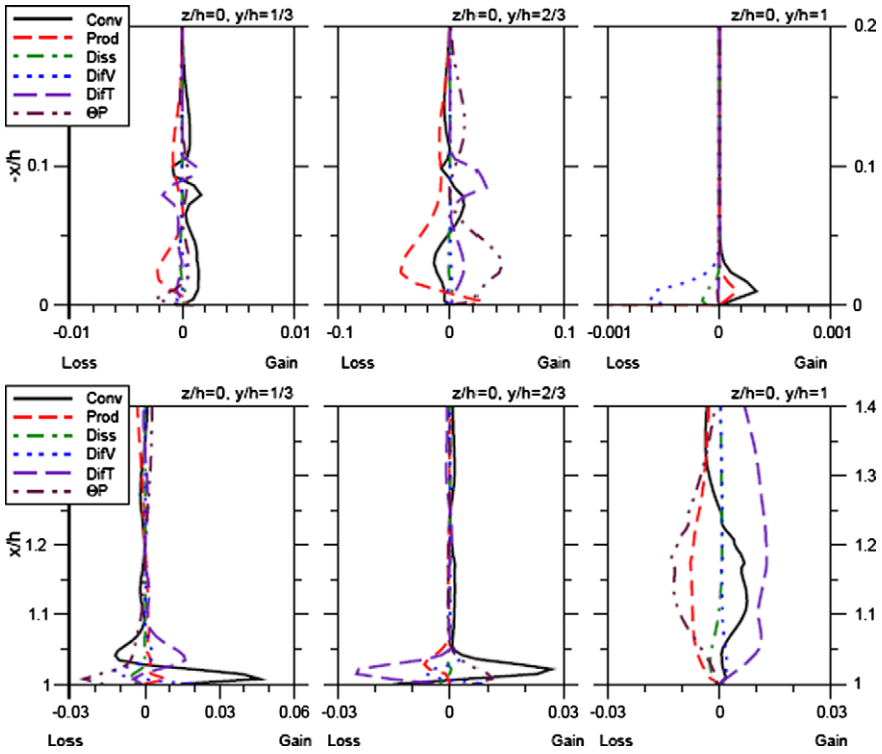

Fig. 22. Profiles of the $u\theta$ budget behind the back face of the cube *C3* (top) and the $w\theta$ budget in front of the front face of the cube *C3* (bottom) in the vertical midplane $z/h = 0$.

it undergoes a very strong shearing. This implies a high production, which is counterbalanced by the turbulent pressure and velocity diffusion.

A high turbulent shear stress is found also at the trailing edge of the top face of the cube. Hence, the same scenario applies to that region as well. The lateral channel flow creates the edge vortex *EV* on the side face of the cube, and the energy transfer is related to the behaviour of this structure. The production of the flux components remains negative in the region along the entire leading edge of the cube, so the dominant term in this region is again the temperature-pressure gradient correlation. Unlike in the impingement zone, at the side corner of the cube the convection is rather strong, as well as the turbulent diffusion. Only very close to the solid boundary along all the faces of the cube the viscous diffusion and the dissipation are contributing to the energy budget balance.

It is evident that the convection is the dominant heat transfer mechanism around the cube *C3*, and the strongest counterbalancing effect is the production. Convective transport is very intensive also in the region behind the cube. Similar to the production of the normal turbulent stresses, the production of heat fluxes is also negative in the region of a high pressure. Namely, under the stabilising flow conditions the energy of the small scales is transferred back into the large scale eddies. This reverse energy transfer from the turbulent to the bulk motion, which must be associated with the reverse cascade in the turbulence spectrum, has been confirmed both experimentally (Geers et al. [18]) and numerically (Hadžiabdić and Hanjalić, [5]) in the stagnation region of a round impinging jet, where a locally negative production of the turbulent kinetic energy was detected in the region around the impingement centre. Fig. 22 shows that in both impingement zones, on the top face of the cube and on the bottom wall just in front of the cube, the production term is negative.

Unlike for the turbulent stresses, in the region of massive separation behind the cube the contribution of the turbulent diffusion to the heat transfer budget is relatively high. In the regions where the shearing is not very strong, such as the wake of the cube, it is the temperature-pressure gradient correlation term that counterbalances the convection. The viscous diffusion and the dissipation terms are generally very small, except for very close to the surface of the cube. The viscous contribution to the transport of both the heat and momentum fluxes is smaller than the other mechanisms and is confined very close to the wall. This is seen in the plot of the budget-terms profiles in Fig. 22 for the $u\theta$ and $w\theta$. More information and discussion can be found in Popovac [9].

4. Conclusions

Vortex morphology and its correlation with the conjugate heat transfer in a configuration mimicking electronics cooling has been investigated using the results of a wall-resolved large-eddy simulation (LES) of velocity and temperature fields. The configuration considered consisted of five in-lined cubes mounted on the bottom wall of a plane channel, of which the central cube – consisting of an internally-heated copper core and a protective low-conducting epoxy layer, was cooled simultaneously the channel crossflow and a normally impinging round jet. The complex interactions of the two fluid streams and cubes generate several characteristic vortex systems in the jet and around the cube, which govern the local heat transfer on the cube surface. The most influential are the periodic vortex rings created naturally in the jet shear layer prior to its impingement on the cube, the separation bubble and the corner eddy on the front face, the edge vortex on the side face, a vortex street generated in the shear layer separating from the top leeward edge of the cube, and the arch vortex created in the massively separated near-wake behind the cube.

In the configuration here considered, with the jet axis displaced upstream by half cube length to coincide with the cube front face, the jet is deflected downstream by the crossflow and fully flushes the impinged cube so that the impingement covers the whole top face of the cube. Furthermore, the vortex rings that break up prior or after the impingement on the cube (both events have been detected) enhance the re-establishing of the wall thermal boundary layer on the top surface, enhancing significantly the heat removal from the cube as a whole. The upstream displacement of the jet ensures that the front face of the cube is well cooled too. Furthermore, due to the interaction between the impinging jet and the lateral crossflow, the edge vortices are created on the side faces of the cube, hence their cooling is also improved because they are flushed with fresh surrounding fluid.

The worst cooling is found on the back face. First, effective cooling is diminished because the fresh fluid can hardly reach the back face of the cube. This is due to the establishing of the arch vortex behind the cube, which traps and recirculates the hot fluid in that region. Second, because of the unsteady character of the arch vortex behind the cube, hot spots created by poor cooling are migrating over the back face. Although less pronounced than in the case without jet (when the cube is cooled solely by the crossflow), this issue is a matter of concern, because the satisfactory cooling of an electronic component should ensure not only high heat removal, but also relatively evenly distributed heat flux over the whole surface of the cooled object.

The computed time-average turbulent stress and the corresponding heat flux components indicate a close link between the turbulent momentum and heat transfer both in boundary layers on the cube and in the separating regions and coherent vortex structures around the cube. This was expected, because the temperature was treated as a passive scalar. The qualitative similarity between the budgets of the heat fluxes and turbulent stresses confirm that the same mechanisms govern the momentum and heat transfer.

Acknowledgements

The use of the supercomputer facilities at *SARA* Amsterdam was sponsored by the *National Computing Facilities Foundation* (NCF), with financial support of the *Netherlands Organisation for Scientific Research* (NWO). The use of the supercomputer facilities at *CINECA* Bologna was sponsored by the EU project *HPC Europa* (Research Infrastructure Action RII3-CT-2003-506079). Both supports are gratefully acknowledged.

References

[1] M. Tummers, K. Hanjalić, R. Rodnik, M. Flikweert, B. Moshfegh, Impinging jet cooling of wall mounted cubes, in: W. Rodi et al. (Eds.), Engineering Turbulence Measurements and Modeling, vol. 6, Elsevier, 2005, pp. 773–782.
[2] M. Popovac, K. Hanjalić, Large-eddy simulations of flow over a jet-impinged wall-mounted cube in a cross stream, Int. J. Heat Fluid Flow 28/6 (2007) 1360–1378.
[3] B. Ničeno, A. Dronkers, K. Hanjalić, Turbulent heat transfer from a multi-layered wall mounted cubes: a large eddy simulation, Int. J. Heat and Fluid Flow. 23 (2002) 173–185.
[4] B. Ničeno, K. Hanjalić, Unstructured large-eddy and conjugate heat transfer simulations of wall bounded flows, in: M. Faghri, B. Sunden (Eds.), Modeling and Simulation of Turbulent Heat Transfer, WIT Press, 2005 (Chapter 2).
[5] M. Hadžiabdić, K. Hanjalić, Vortical structures and heat transfer in a round impinging jet, J. Fluid Mech. 596 (2008) 221–260.
[6] M. Flikweert, Flow and heat transfer investigation of wall-mounted cubes in cross-flow, M.Sc. thesis, Delft University of Technology, Delft, The Netherlands, 2005.
[7] E.R. Meinders, K. Hanjalić, Vortex structure and heat transfer in turbulent flow over a wall-mounted matrix of cubes, Int. J. Heat Fluid Flow 20 (1999) 255–267.
[8] N. Kasagi, A. Kuroda, M. Hirata, Numerical investigation of near-wall turbulent he at transfer taking into account the unsteady heat conduction in the solid wall, ASME J. Heat Transfer 111 (1989) 385–392.

[9] M. Popovac, Modelling and simulation of turbulence and heat transfer in wall-bounded flows, Ph.D. thesis, Delft University of Technology, Delft, The Netherlands, 2006.
[10] M. Germano, U. Piomelli, P. Moin, W.H. Cabot, A dynamic subgrid-scale eddy viscosity model, Phys. Fluids A 3 (1991) 1760–1765.
[11] A. Rivero, J.A. Ferre, F. Giralt, Organized motions in a jet in cross-flow, J. Fluid Mech. 444 (2001) 117–149.
[12] R.L. Simpson, Junction flows, Annu Rev. Fluid Mech. 33 (2001) 415–445.
[13] B.D. Patte, W.D. Baines, Profiles of the round turbulent jets in a cross flow, Proc. A.S.C.E. J. Hydraul. Div. 92 (1967) 53–64.
[14] S. Muppidi, K. Mahesh, Study of trajectories of jets in crossflow using direct numerical simulation, J. Fluid Mech. 530 (2005) 81–100.
[15] R. Rajaratnam, Turbulent jets, in: Developments in Water Science, vol. 5, Elsevier, 1976.
[16] E. Gutmark, C.M. Ho, Preferred modes and the spreading rates of jets, Phys. Fluids 26 (1983) 2932–2938.
[17] E.R. Meinders, Experimental study of heat transfer in turbulent flows over wall-mounted cubes, Ph.D. thesis, Delft University of Technology, 1998.
[18] L. Geers, K. Hanjalić, M. Tummers, Wall imprints of turbulent structure and heat transfer in multiple impinging jet arrays, J. Fluid Mech. 546 (2006) 255–284.